PERGAMON

Journal of Structural Geology 23 (2001) 789–801

JOURNAL OF STRUCTURAL GEOLOGY

www.elsevier.nl/locate/jstrugeo

Breddin's graph for tectonic regimes

Bernard Célérier*, Michel Séranne

Institut des Sciences de la Terre de l'Eau et de l'Espace de Montpellier, Université de Montpellier II-CNRS, case courrier 57, 34095 Montpellier Cedex 5, France

Received 4 August 1999; accepted 2 August 2000

Abstract

A simple graphical method is proposed to infer the tectonic regime from a fault and slip data set. An abacus is overlaid on a plot of the rake versus strike of the data. This yields the horizontal principal stress directions and a constraint on the stress tensor aspect ratio, in a manner similar to Breddin's graph for two-dimensional strain analysis. The main requirement is that one of the principal stress directions is close to the vertical. This method is illustrated on monophase synthetic and natural data, but is also expected to help sort out multiphase data sets.

1. Introduction

Fault and slip or earthquake focal mechanism data are one of the most commonly available stress indicators (Zoback, 1992). The relationship between these indicators and stress is straightforward when the fault plane is created by the same stress system that also controls the slip direction (Anderson, 1905; Bucher, 1920, 1921). When a pre-existing fault is reactivated the relationship is non-unique and provides only limited constraints on the state of stress (Wallace, 1951; Bott, 1959; McKenzie, 1969; Célérier, 1988). In those cases a state of stress shared by multiple fault and slip data is usually sought by inverse methods (Carey and Brunier, 1974; Angelier, 1984; Etchecopar et al., 1981; Vasseur et al., 1983; Gephart and Forsyth, 1984; Michael, 1984; Reches, 1987). Two major difficulties in this approach are (1) to separate the data into subsets that correspond to a homogeneous stress system and (2) to evaluate how well each subset constrains the stress system. Recent work has focused on graphical representations to address these problems (Simón Gómez, 1986; Fry, 1992, 1999). A systematic study of the geometrical properties of stress systems (Célérier, 1995) suggests a simple graphical method easily applicable when one principal stress axis is vertical. The goal of this paper is to present and illustrate this method through a few simple synthetic and natural cases.

2. Theory

2.1. Shear stress orientation

The stress tensor is classically defined by the principal stress directions, $\vec{s}_1$, $\vec{s}_2$, $\vec{s}_3$, and magnitudes, $\sigma_1 \geq \sigma_2 \geq \sigma_3$, with the rock mechanics convention that compressive stresses are positive. When one of the principal stresses is vertical, it is convenient to define the frame $V = (\vec{s}_{h1}, \vec{s}_{h2}, \vec{s}_v)$, where $\vec{s_{h1}}$ is the maximum horizontal principal stress direction, $\vec{s_{h2}}$ is the minimum horizontal principal stress direction and $\vec{s}_v$ is vertical and points downward so that the frame is direct (Fig. 1 and Table 1). The corresponding eigenvalues, σ_{h1}, σ_{h2}, σ_v, verify $\sigma_{h1}\ \varepsilon\ \sigma_{h2}$ and are combined to introduce the tectonic regime parameter γ:

$$\gamma = \frac{\sigma_{h1} + \sigma_{h2} - 2\sigma_v}{\sigma_{h1} - \sigma_{h2}} \qquad \gamma \in [-\infty, +\infty]. \tag{1}$$

This parameter varies from $-\infty$ to $+\infty$ as the tectonic regime varies from radial extension to wrench and then to radial compression (Fig. 2) and is related to the stress tensor aspect ratio r_0:

$$r_0 = \frac{\sigma_1 - \sigma_2}{\sigma_1 - \sigma_3} \qquad r_0 \in [0, 1] \tag{2}$$

as given in Table 2. The tectonic regime (Harland and Bayly, 1958) can be defined either by (r_0, i_{sv}), where i_{sv} is the index of the vertical principal stress, i.e. $\sigma_v = \sigma_{isv}$ with isv = 1, 2 or 3 (Philip, 1987; Guiraud et al., 1989), or by the value of γ that contains both pieces of information (Armijo et al., 1982).

A frame of reference, $N = (\vec{n}_1, \vec{n}_2, \vec{n}_3)$, is attached to

* Corresponding author. Tel.: +33-(0)4-67-14-39-06; fax: +33-(0)4-67-14-47-74.

E-mail address: Bernard.Celerier@dstu.univ-montp2.fr (B. Célérier).

0191-8141/01/$ - see front matter
PII: S0191-8141(00)00140-1

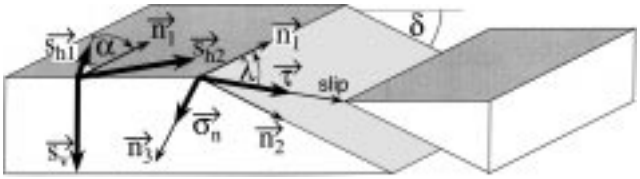

Fig. 1. Slip vector orientation with respect to the principal stress frame $V = (\vec{s}_{h1},\ \vec{s}_{h2},\ \vec{s}_v)$ and fault plane frame, $N = (\vec{n}_1,\ \vec{n}_2,\ \vec{n}_3)$; the slip is assumed to be parallel to the shear stress $\vec{\tau}$. The variables are defined in Table 1.

fault plane frame with $\vec{n}_1$ along the strike and so that the plane dips to its right side, $\vec{n}_2$ along the dip, and $\vec{n}_3$ the downward pointing normal (Fig. 1). The fault plane orientation is then defined by its dip, δ, and its strike, α, with respect to the largest horizontal principal stress direction, i.e. the angle between $\vec{s}_{h1}$ and $\vec{n}_1$.

Table 1
Symbols

Symbols	Comments
	Fault plane and slip direction
$N = (\vec{n}_1, \vec{n}_2, \vec{n}_3)$	fault plane frame: $\vec{n}_1$ is along the strike so that the dip is towards its right, $\vec{n}_2$ along the dip and $\vec{n}_3$ is the downward normal (Fig. 1)
α	fault plane strike with respect to $\vec{s}_{h1}$, i.e. angle $(\vec{s}_{h1}, \vec{n}_1)$ (Fig. 1)
δ	fault plane dip (Fig. 1)
λ	rake of slip, i.e. angle $(\vec{\tau}, \vec{n}_1)$ defined in $[-180, +180]$ (Fig. 1)
	Stress tensor
$\vec{s}_1, \vec{s}_2, \vec{s}_3$	principal stress directions (eigenvectors of the stress tensor)
$\sigma_1 \geq \sigma_2 \geq \sigma_3$	principal stress magnitudes (eigenvalues of the effective stress tensor)
r_0	tensor aspect ratio or relative position of σ_2 (Eq. (2))
$V = (\vec{s}_{h1}, \vec{s}_{h2}, \vec{s}_v)$	maximum horizontal, minimum horizontal and vertical principal stress frame (Fig. 1)
σ_{h1}, σ_{h2}, σ_v	maximum horizontal, minimum horizontal and vertical principal stress magnitudes: $\sigma_{h1} \geq \sigma_{h2}$
γ	tectonic regime parameter (Eq. (1))
i_{sv}	index of the vertical principal stress: $\sigma_v = \sigma_{isv}$. $i_{sv} = 1, 2, 3$ for extensional, wrench and compressional regimes respectively (Fig. 2)
	Applied stress
$\vec{F}$	stress applied to the footwall (Eq. (3))
$\vec{\tau}_d$	shear stress direction (without magnitude information) (Eq. (5))
	Other
$k(\alpha, \gamma) \in \{-1, 0, 1\}$	signed integer (given in Fig. 2) used in Eq. (6) to obtain the rake, λ
$B_\delta(r_0, i_{sv})$	domain of all strike and rake combinations, (α, λ), compatible with regime (r_0, i_{sv}) and dip greater than δ
$NB_\delta(r_0, i_{sv})$	normal subdomain of all strike and rake combinations, (α, λ), compatible with regime (r_0, i_{sv}) and dip greater than δ
$RB_\delta(r_0, i_{sv})$	reverse subdomain of all strike and rake combinations, (α, λ), compatible with regime (r_0, i_{sv}) and dip greater than δ

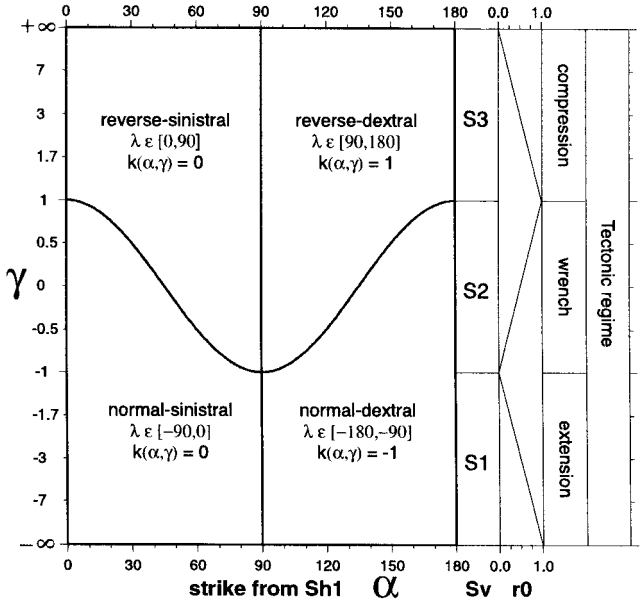

Fig. 2. Tectonic style of reactivation and corresponding rake intervals as a function of the fault plane strike, α, with respect to the maximum horizontal principal stress direction, $\vec{s}_{h1}$, and of the tectonic regime, γ. The vertical axis is linear with respect to r_0, not with respect to γ. The value of $k(\alpha,\gamma)$ is that to use in Eq. (6) to obtain λ.

The matrix in the N frame, F^N, of the stress $\vec{F}$ applied to the footwall of interior normal $\vec{n}_3$ is (a detailed derivation can be found in Célérier, 1995):

$$F^N = \sigma_{h2}\begin{bmatrix}0\\0\\1\end{bmatrix} + (\sigma_{h1} - \sigma_{h2}) \times \begin{bmatrix} \frac{1}{2}\sin 2\alpha \sin\delta \\ \frac{1}{4}(\cos 2\alpha - \gamma)\sin 2\delta \\ \frac{1-\gamma}{2} - \frac{1}{2}(\cos 2\alpha - \gamma)\sin^2\sigma \end{bmatrix} \quad (3)$$

The first component is the shear stress strike component, the second component is the shear stress dip component, and the third component is the normal stress. Because

$$(\sigma_{h1} - \sigma_{h2})\sin\delta \geq 0 \quad (4)$$

Table 2
Tectonic regimes and stress tensor aspect ratio

Regime	σ_v	Interval of γ	γ	r_0
compression	σ_3	$]+1, +\infty[$	$\gamma = \frac{2}{r_0} - 1$	$r_0 = \frac{2}{1+\gamma}$
wrench	σ_2	$[-1, +1]$	$\gamma = 2r_0 - 1$	$r_0 = \frac{1+\gamma}{2}$
extension	σ_1	$[-\infty, -1]$	$\gamma = -\frac{1+r_0}{1-r_0}$	$r_0 = -\frac{1+\gamma}{1-\gamma}$

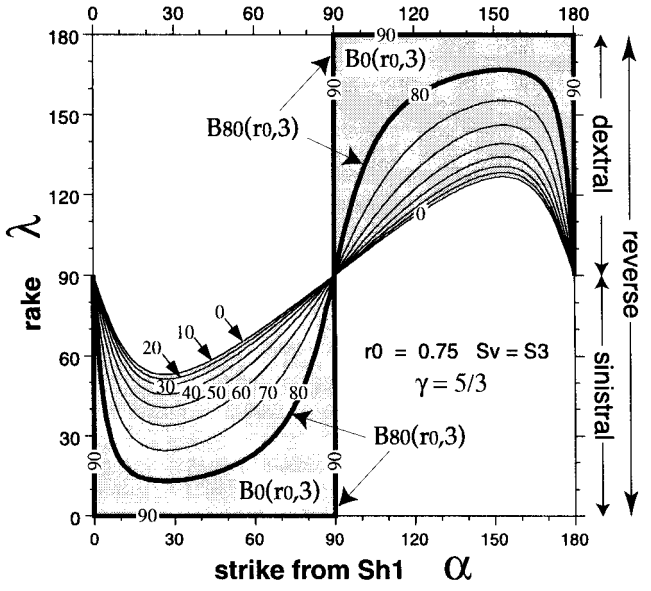

Fig. 3. Variation of rake as a function of strike for fault planes of fixed dip in a typical compressional tectonic regime: $\gamma = 5/3$ or $r_0 = 0.75$. The 10 curves correspond to fixed dips from 0° to 90° by increments of 10°; the curve label indicates the dip. Slip is pure dip-slip when the plane strikes along $\vec{s}_{h1}$ or $\vec{s}_{h2}$. It becomes shallower for other strikes.The domain $B_0(r_0, 3)$ of all the possible combinations of strike, α, and rake, λ, in the fixed regime(r_0, 3) is stippled. It is bounded by the curve for $\delta = 0°$ and by that for $\delta = 90°$. The boundaries of the domain $B_{80}(r_0, 3)$ of all the possible combinations of strike, α, and rake, λ, for planes dipping more than 80° in the fixed regime (r_0, 3) correspond to the curve for $\delta = 80°$ and for $\delta = 90°$ and are thickened.

the shear stress always points in the same direction as the vector $\vec{\tau}_d$ defined by:

$$\tau_d^N = \begin{bmatrix} \tau_{d1} \\ \tau_{d2} \\ 0 \end{bmatrix} = \begin{bmatrix} \sin 2\alpha \\ (\cos 2\alpha - \gamma)\cos\delta \\ 0 \end{bmatrix}. \quad (5)$$

Because the vector $\vec{\tau}_d$ is unchanged if strike is shifted by 180°, the range of strike will be restricted to [0°, 180°] in what follows.

The slip vector of the hanging wall relative to the footwall will be assumed to be parallel to the shear stress applied to the footwall, thus to $\vec{\tau}_d$ (Wallace, 1951; Bott, 1959; McKenzie, 1969). The type of movement is therefore determined by the signs of the components of $\vec{\tau}_d$ and does not depend on the fault plane dip, δ (Fig. 2).

The rake of slip, λ, is defined as in Aki and Richards (1980); p. 106) as the angle between the slip vector and the fault plane strike direction, $\vec{n}_1$ (Fig. 1). It is the opposite of the polar angle of $\vec{\tau}_d$ in the N frame and can be computed as a function of γ, α and δ by:

$$\lambda(\alpha, \delta, \gamma) = \text{atan}\left[\frac{\gamma - \cos 2\alpha}{\sin 2\alpha}\cos\delta\right] + k(\alpha, \gamma)180° \quad (6)$$

where k(α,γ) is either 0, 1, or −1, as given in Fig. 2, and the angles are in degrees.

Eq. (5) and Eq. (6) show that the fault plane orientation, α and δ, and the tectonic regime, γ, fully determine the slip orientation as demonstrated by Bott (1959). If the tectonic regime is fixed, the rake of slip, λ, depends solely on the fault plane orientation. A series of curves that represent the rake, λ, as a function of the fault plane strike, α, for a fixed value of the dip, δ, illustrate this dependency for three typical values of γ (Figs 3, 4 and 5). To facilitate the following discussion, slip directions close to strike-slip and dip-slip will be called shallow and steep respectively.

2.2. Compressional regime

In the case of a compressional regime ($i_{sv} = 3$ or $\gamma > 1$, Fig. 3) the steepest slip is pure reverse ($\lambda = 90°$) and occurs when the plane strikes along one of the horizontal principal stress directions ($\alpha = 0°$ or $\alpha = 90°$) whatever its dip. For planes of equal dip the slip becomes shallower as the plane strikes away from the horizontal principal stress direction. For planes of equal strike the slip becomes shallower as the plane dip increases. The shallowest slips are pure strike-slip and are obtained for vertical planes independently of their strike. As a consequence we can define the domain $B_0(r_0, 3)$ (the shaded area of Fig. 3) of all the strike and rake, (α, λ), compatible with the tectonic regime (r_0, $i_{sv} = 3$). In other words, the slip data from a set of faults reactivated in the tectonic regime (r_0, $i_{sv} = 3$) should fall into the domain $B_0(r_0, 3)$. This domain is bounded towards strike-slip by the curves corresponding to the vertical planes ($\delta = 90°$) and towards dip-slip by the curves corresponding to the horizontal planes ($\delta = 0°$).

As the stress tensor aspect ratio, r_0, increases (and γ decreases), the strike slip boundary of $B_0(r_0, 3)$ remains

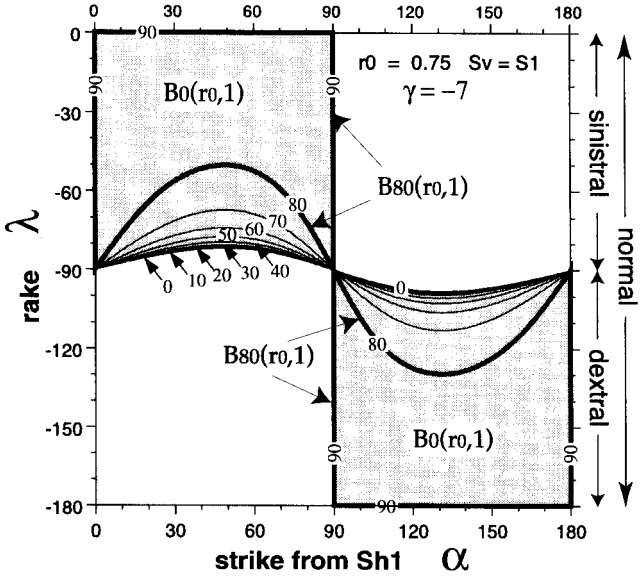

Fig. 4. Variation of rake as a function of strike for fault planes of fixed dip in a typical extensional tectonic regime: $\gamma = -7$ or $r_0 = 0.75$. Same conventions as Fig. 3.

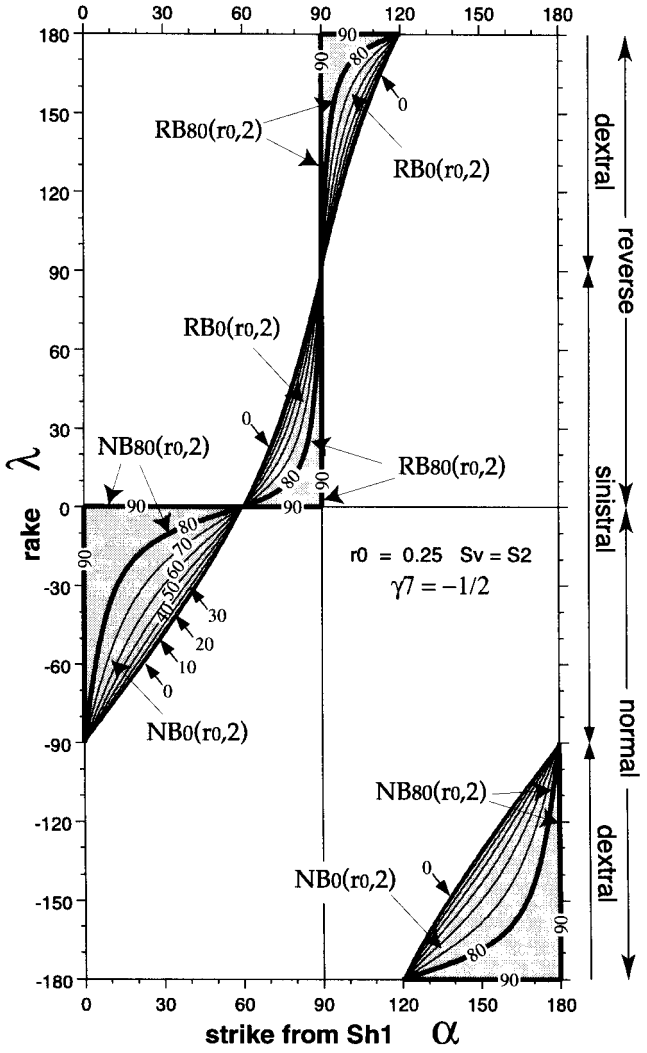

Fig. 5. Variation of rake as a function of strike for fault planes of fixed dip in a typical wrench tectonic regime: $\gamma = -0.5$ or $r_0 = 0.25$. Same conventions as Fig. 3. The domain $B_0(r_0, 2)$ is the reunion of a normal movement, $NB_0(r_0, 2)$, and a reverse movement, $NB_0(r_0, 2)$, subdomains.

unchanged whereas the dip-slip boundary moves towards strike-slip so that the resulting set of domains are included in each other (Fig. 6):

$$0 \le r_{01} \le r_{02} \le 1 \Rightarrow B_0(r_{02}, 3) \subset B_0(r_{01}, 3). \quad (7)$$

This geometrical property means that as the tectonic regime evolves towards a wrench regime, the strike component of slip increases on planes striking away from the principal stress directions.

2.3. Extensional regime

The situation for extensional regime ($i_{sv} = 1$ or $\gamma < -1$, Fig. 4) is symmetrical to that for compressional regime: changing γ into $-\gamma$ and α into $90° - \alpha$ yields same strike component but opposite dip components of the slip direction (Eq. (5)), therefore opposite rake (Eq. (6)). The domains $B_0(r_0, 1)$ are symmetrical to those for compressional regime and are included in the reverse order (Fig. 7):

$$0 \le r_{01} \le r_{02} \le 1 \Rightarrow B_0(r_{01}, 1) \subset B_0(r_{02}, 1). \quad (8)$$

Note that in the extensional and compressional regimes the domains $B_0(r_0, 1)$ and $B_0(r_0, 3)$ are restricted to the range of normal oblique and reverse oblique rakes respectively.

2.4. Wrench regime

In the case of a wrench regime ($i_{sv} = 2$, or $1 > \gamma > -1$, Fig. 5) the slip is pure normal ($\lambda = -90°$) when the plane strikes along the maximum horizontal principal stress direction ($\alpha = 0°$) and pure reverse ($\lambda = +90°$) when the plane strikes along the minimum horizontal principal stress direction ($\alpha = 90°$) whatever its dip. Again, at constant dip, the slip becomes shallower as the plane strikes away from the horizontal principal stress direction, but there is now a strike for which slip is pure strike slip whatever the plane dip. For planes of equal strike the slip becomes shallower as the plane dip increases, similarly to what happens in the other two regimes.

The domain of all the slip distribution compatible with the tectonic regime (r_0, 2), $B_0(r_0, 2)$, remains bounded towards strike-slip by the curves corresponding to the vertical planes ($\delta = 90°$) and towards dip-slip by the curves corresponding to the horizontal planes ($\delta = 0°$) (Fig. 5). This domain now spans the whole range of oblique rakes (Fig. 5).

As the stress tensor aspect ratio, r_0, decreases from 1 to 0 (and γ decreases from 1 to -1, Fig. 2 and Table 2), the strike slip boundary of $B_0(r_0, 2)$ remains unchanged and the dip slip boundary evolves (Fig. 8). However because the dip slip and strike slip boundaries now intersect, it is convenient to subdivide the domain $B_0(r_0, 2)$ into two parts (Fig. 5): one part, $RB_0(r_0, 2)$, corresponds to the reverse movements ($0° < \lambda < +180°$), and the other part, $NB_0(r_0, 2)$, corresponds to the normal movements ($-180° < \lambda < 0°$), so that

$$B_0(r_0, 2) = RB_0(r_0, 2) \cup NB_0(r_0, 2). \quad (9)$$

The part $RB_0(r_0, 2)$ follows the inclusion rule:

$$0 \le r_{01} \le r_{02} \le 1 \Rightarrow RB_0(r_{01}, 2) \subset RB_0(r_{02}, 2) \quad (10)$$

whereas the part $NB_0(r_0,2)$ follows:

$$0 \le r_{01} \le r_{02} \le 1 \Rightarrow NB_0(r_{02}, 2) \subset NB_0(r_{01}, 2). \quad (11)$$

The apparent complexity of the inclusion relationships of Eq. (7), Eq. (8), Eq. (10), and Eq. (11) is partly due to the fact that r_0 reverses its sense of variation as the tectonic regime evolves (Fig. 2). As the tectonic regime evolves from radial compression to radial extension and γ decreases continuously from $-\infty$ to $+\infty$, the part of $B_0(r_0, i_{sv})$ that corresponds to reverse dip component of slip shrinks whereas the part that corresponds to normal dip component of slip expands.

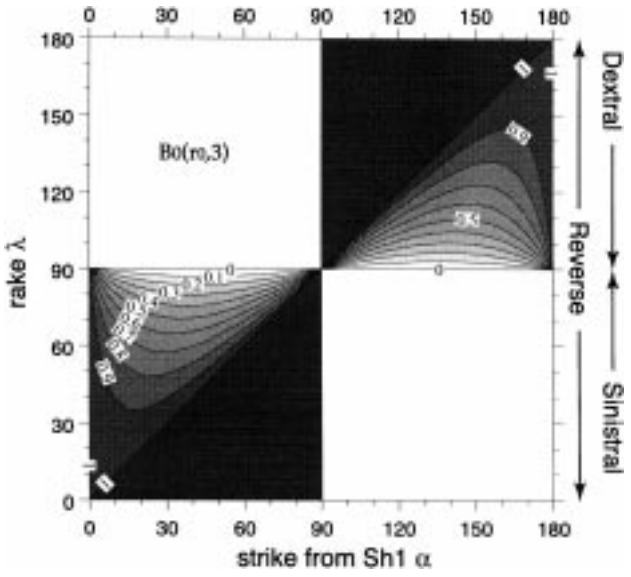

Fig. 6. Set of the domain $B_0(r_0, 3)$ of all the possible combinations of strike, α, and rake, λ, in the fixed compressional regime (r_0, 3) for values of r_0 incremented by 0.1. The boundary curve label indicates r_0. Each domain includes those darker than itself.

2.5. Breddin's graph

Putting the different $B_0(r_0, i_{sv})$ boundaries (Figs 6–8) together on the same graph yields an abacus (Fig. 9). We will refer to this abacus as Breddin's graph for tectonic regime both because some of the curves are identical to those of Breddin's graph used for two dimensional strain analysis (Breddin, 1956; Ramsay and Huber, 1985) and because it will be used in an similar fashion. Clearly,

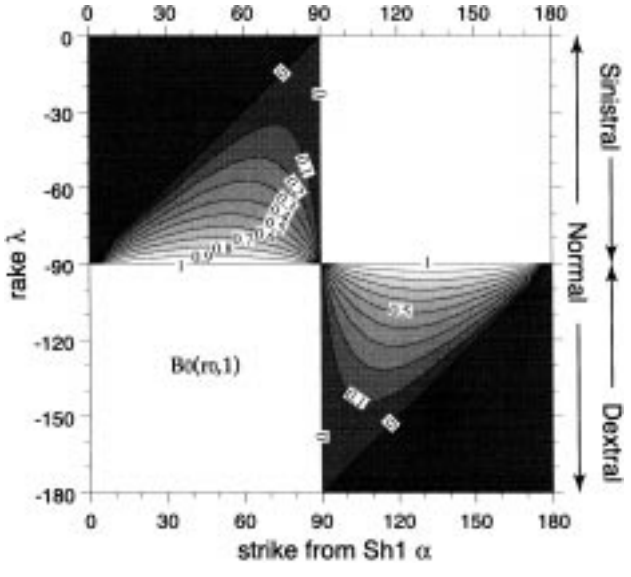

Fig. 7. Set of the domain $B_0(r_0, 1)$ of all the possible combinations of strike, α, and rake, λ, in the fixed extensional regime(r_0, 1) for values of r_0 incremented by 0.1. The boundary curve label indicates r_0. Each domain includes those darker than itself.

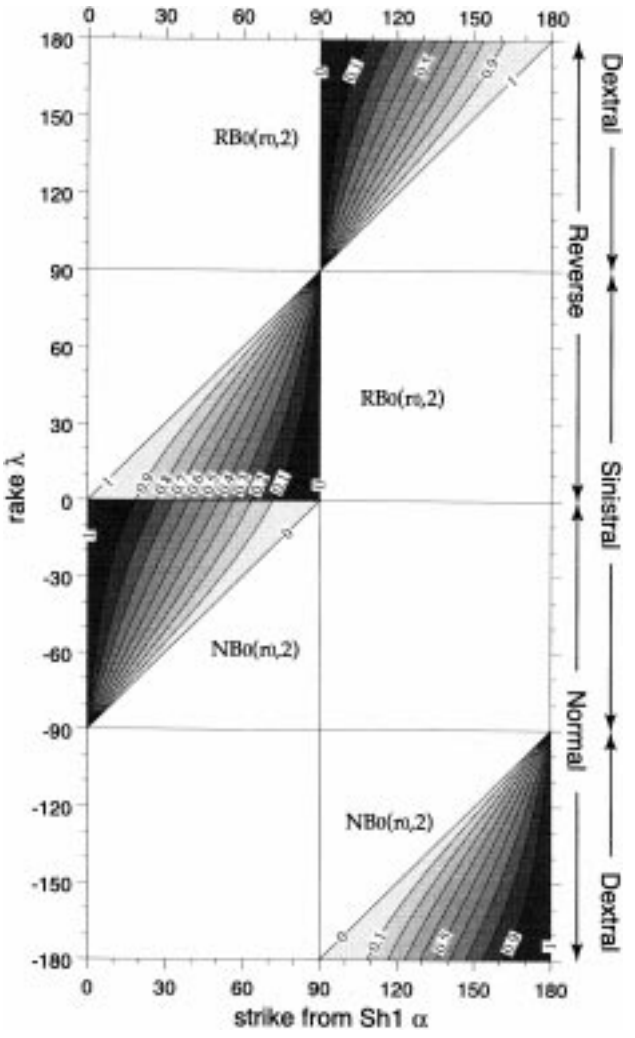

Fig. 8. Set of the domain $B_0(r_0, 2)$ of all the possible combinations of strike, α, and rake, λ, in the fixed wrench regime (r_0, 2) for values of r_0 incremented by 0.1. The boundary curve label indicates r_0. Each domain is subdivided into its normal, $NB_0(r_0, 2)$, and reverse, $NB_0(r_0, 2)$, subdomain. Each subdomain includes those darker than itself.

we cannot expect the three-dimensional stress problem addressed here to be treated as simply as the two-dimensional strain problem addressed by Breddin (1956) without simplifications. The first simplification leading to the graph of Fig. 9 consists of ignoring the influence of the fault plane dip on the rake of slip. A data set where all the fault planes dip more than 80° does not span the whole $B_0(r_0, i_{sv})$ zone, limited by the 0° dip curves but rather the smaller $B_{80}(r_0, i_{sv})$ zone limited by the 80° dip curves (Figs 3, 4 and 5). In such a case the proper abacus needs to be drawn with the set of the 80° dip limiting curves (Fig. 10). However, because of the inclusion relationships, using the abacus of Fig. 9 instead of that of Fig. 10 turns out to provide a looser constraint on the sought stress regime but not to be a major impediment as we will see further down.

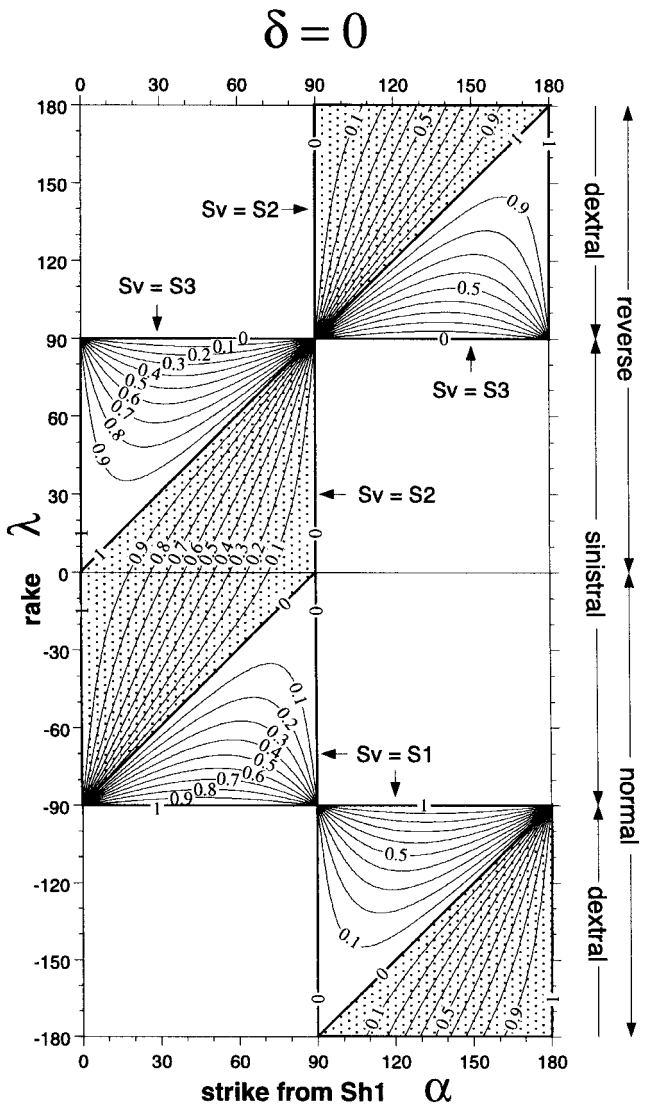

Fig. 9. Breddin's graph for tectonic regimes. The boundaries of $B_0(r_0, i_{sv})$ are drawn for values of r_0 varying from 0 to 1 by increments of 0.1 and for $i_{sv} = 1$, 2 and 3; the boundary labels indicate the value of r_0 and the zone covered by boundaries corresponding to the wrench regime ($i_{sv} = 2$) is dotted. This graph can be superposed to a simple rake versus geographical azimuth data plot: data collected in regime (r_0, i_{sv}) should fall in the $B_0(r_0, i_{sv})$ domain after the proper azimuth translation that brings the origin of the graph against the geographical azimuth of the maximum horizontal principal stress direction; r_0 is constrained by choosing the domain that most closely bounds the data.

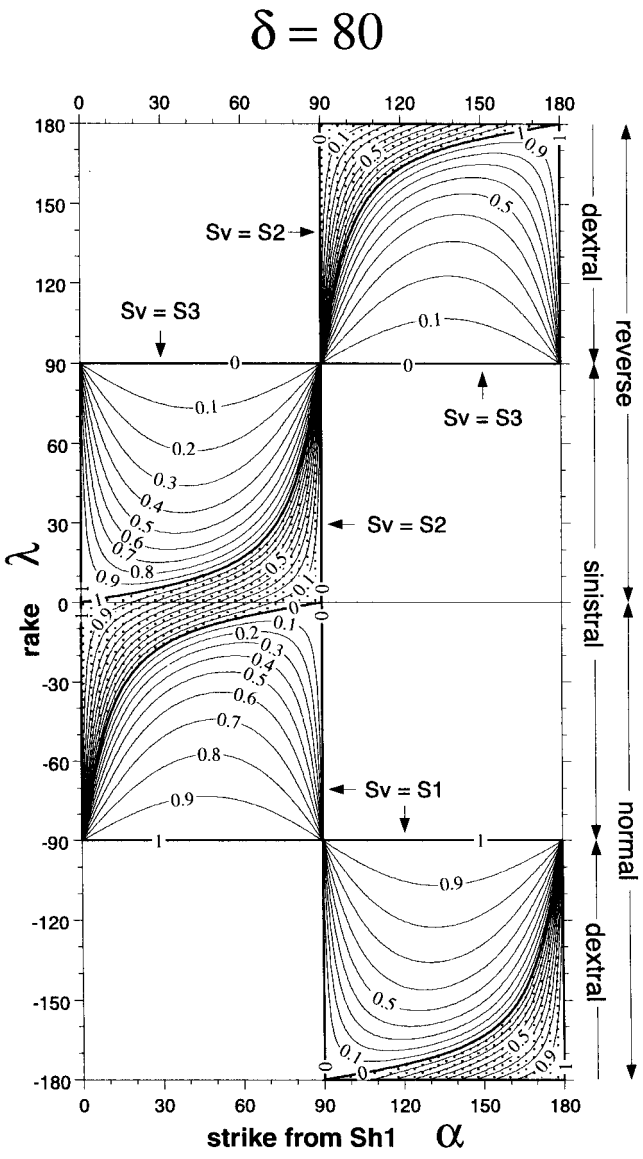

Fig. 10. Altered Breddin's graph for tectonic regimes for planes of dip larger than 80°. The boundaries of $B_{80}(r_0, i_{sv})$ (defined in Figs 3, 4 and 5) are drawn for values of r_0 varying from 0 to 1 by increment of 0.1 and for $i_{sv} = 1$, 2 and 3. The boundary labels indicate the value of r_0 and the zone covered by the boundaries corresponding to the wrench regime ($i_{sv} = 2$) is dotted. Data dipping at more than 80° collected in regime (r_0, i_{sv}) should fall in the now reduced $B_{80}(r_0, i_{sv})$ domain after the proper azimuth translation. Data corresponding to $\delta = 80°$ should fall along the curved boundary of $B_{80}(r_0, i_{sv})$.

3. Application to synthetic data

3.1. Generation of the data

Synthetic sets of faults are used to illustrate how the geometrical relationships discussed above can be applied to fault and slip data. These sets were generated in two steps.

First a computer procedure generated 100 fault plane orientations uniformly distributed in space (Fig. 11a). To do so the strikes were drawn randomly with a uniform distribution in [0°, 360°] (Fig. 11b) whereas the dips, δ, (Fig. 11c) were generated by

$$\delta = \mathrm{Arccos}(X) \tag{12}$$

where X was drawn randomly with a uniform distribution in [0, 1]. The resulting fault planes are oriented with respect to geographical North (Fig. 11).

Then 3 different stress regimes (C2, C8, and W2, Table 3) were chosen and the predicted rake of slip was computed for each fault plane. These computed rakes were used, without

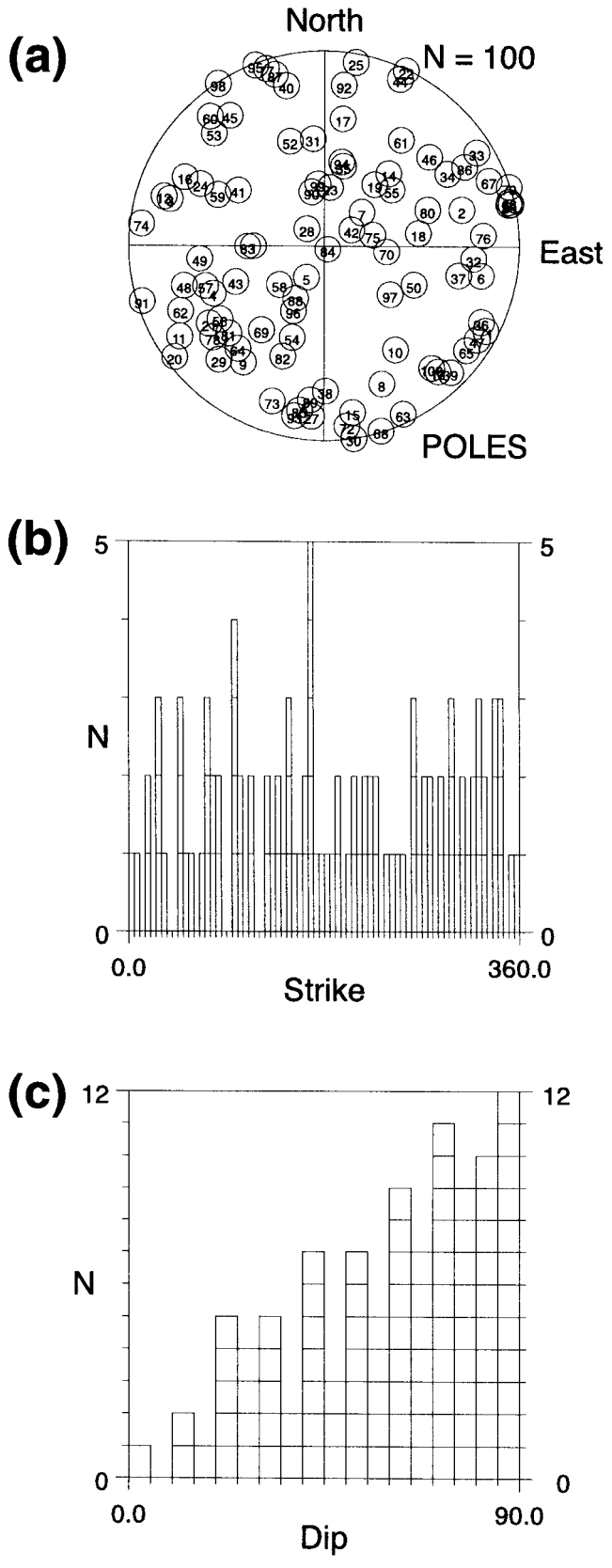

Fig. 11. Synthetic fault plane orientations. (a) Equal area stereographic projection of the poles, lower hemisphere. Fault number is shown within each symbol. (b) Strike histogram with 5° bins. (c) Dip histogram with 5° bins.

adding any noise, to build three fault slip data sets, that also are named C2, C8, and W2, each exactly compatible with a single state of stress.

3.2. Graphical analysis

The analysis of the data is illustrated for the set C8 and proceeds in three steps.

First, the rake of the data is plotted versus the strike with respect to the geographical North (Fig. 12). Because of the shear stress invariance through a 180° strike translation, the strike axis is restricted to the [0°, 180°] interval and data striking outside this interval are brought back into it by subtracting the correct multiple of 180°. The rake is defined in [−180°, +180°] and includes the information about the type of movement.

Second, based on the rake distribution, a decision is made as to which of the three main tectonic regimes will account for most of the data. The fact that the data set C8 is limited to reverse movements suggests a compressional regime.

Third, Breddin's graph (Fig. 9) is laid over the rake versus strike plot. It is then horizontally shifted along the strike axis until one of the $B_0(r_0, 3)$ domains of the expected compressional regime includes most of the data (Fig. 13). In the present synthetic case it is naturally possible to include all of the data.

Because the abacus horizontal axis is built with respect to the maximum principal stress direction whereas the fault data horizontal axis is built with respect to the North, the correspondence between these two axes yields the horizontal principal stress direction (Fig. 13). One can note that this strike adjustment is controlled by the separation between dextral and sinistral data. This is a direct consequence of the fact that the horizontal principal stress directions control the sign of the strike component of slip (Fig. 2 and Eq. (5)).

The dip-slip boundary of the smallest fitting $B_0(r_0, 3)$ domain yields a constraint on the value of r_0. The choice of this boundary is constrained by how close to dip-slip the rake is when the strike is not close to one of the horizontal principal stress direction. This is a direct consequence of the fact that the stress tensor aspect ratio controls how steep slip can be on planes striking away from the horizontal principal stress direction (Eq. (6)). The smallest domain $B_0(r_0, 3)$ that fits the C8 data corresponds to $r_0 = 0.8$. This means that the data require $r_0 \leq 0.8$. To further constrain this parameter would require dip information since the dip slip boundary is reached only for shallow dipping planes.

This control of the tectonic regime on steep slips is illustrated by the contrast between C8 (Fig. 13) and C2 (Fig. 14): in the case of C2 the slips are much steeper, indicating a tectonic regime closer to radial compression and the constraint from the graphical fit becomes $r_0 \leq 0.2$.

In both cases the inferred upper limit of r_0 happens to correspond to the actual value of r_0 used to generate the data set (Table 3). This means that enough shallow dipping

Table 3
Reduced stress tensors

Label	Regime	σ_v	γ	r_0	S1		S2		S3	
					Azimuth	Dip	Azimuth	Dip	Azimuth	Dip
C2	compression	σ_3	9.0	0.2	45°	0°	135°	0°	N/A	90°
C8	compression	σ_2	1.5	0.8	45°	0°	135°	0°	N/A	90°
W2	wrench	σ_1	−0.6	0.2	45°	0°	N/A	90°	135°	0°
BRE1	extension	σ_1	−1.0	1.0	N/A	90°	20°	0°	110°	0°
BRE2	extension	σ_1	≤−1.9	≥0.3	N/A	90°	20°	0°	110°	0°
INV1	extension	σ_1	−1.3	0.13	35.3°	81.2°	−160.9°	8.4°	−70.5°	2.4°
INV2	extension	σ_1	−1.4	0.18	26.3°	79.0°	−160.5°	10.9°	−70.2°	1.3°

planes are present in the data set (Fig. 11) to provide rakes very close to the dip slip boundary.

The data set W2 displays both reverse and normal movements (Fig. 15), and therefore two hypothesis can be made: either the set is monophase and only a wrench regime can account for these diverse movements, or the set is polyphase and combinations of compressional, extensional and wrench regimes may be sought. We will limit the analysis to the monophase hypothesis both because it is simpler, and therefore a very reasonable starting point for any analysis of this type, and because synthetic data provide some hindsight which is difficult to ignore.

Once the principal stress axes are recognized, the constraint on the stress tensor aspect ratio is tighter than in the C2 and C8 cases because the $RB_0(r_0, 2)$ fitting domain

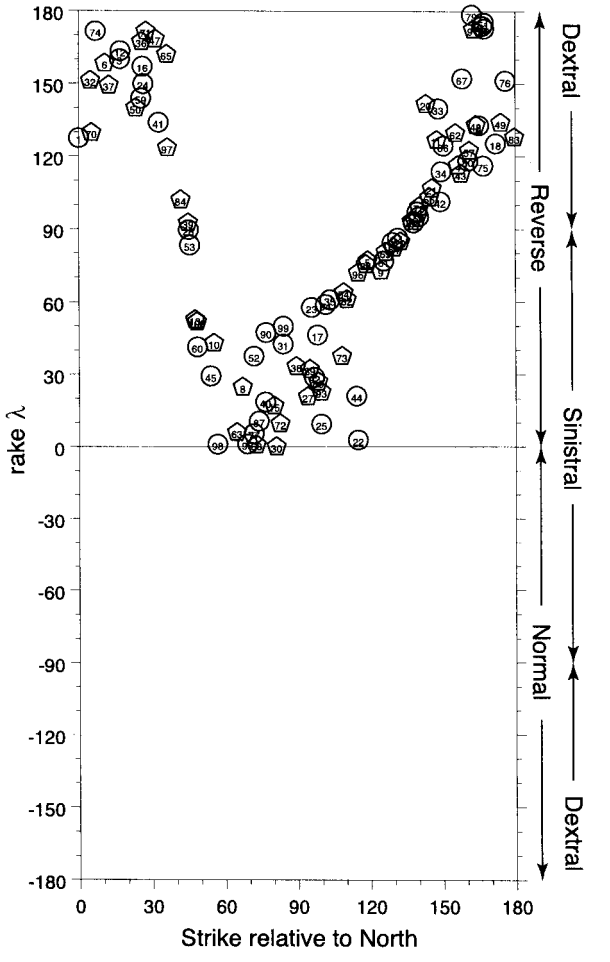

Fig. 12. Rake versus strike plot of data set C8 (Table 3). Pentagons correspond to data with strike outside [0, 180°] that have been translated back into this interval by adding the correct multiple of 180°. Fault numbers shown within each symbol correspond to those of Fig. 11.

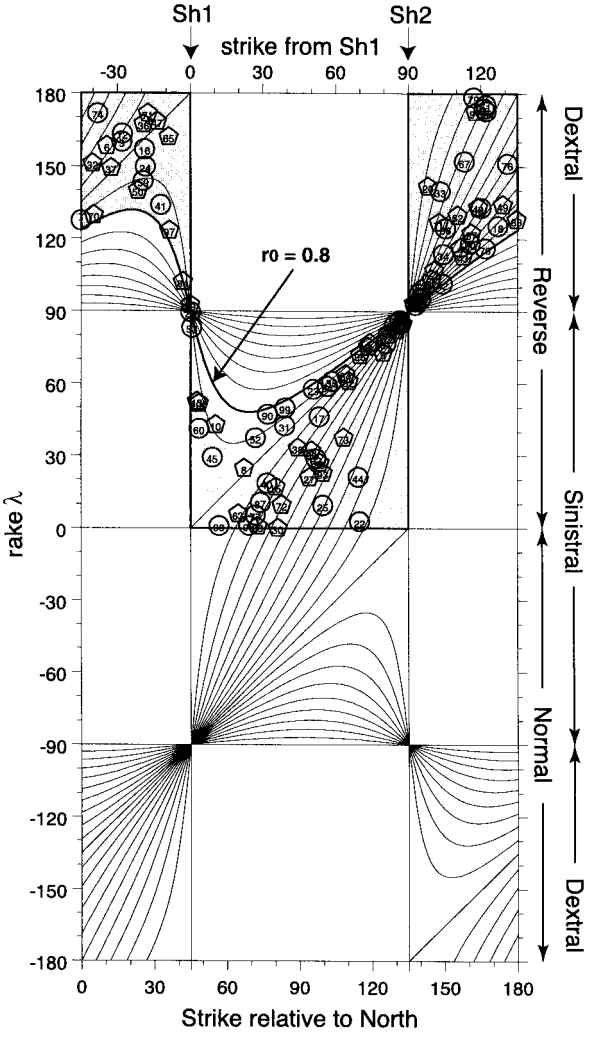

Fig. 13. Rake versus strike plot of data set C8 (Table 3) overlain by properly translated Breddin's graph of Fig. 9.

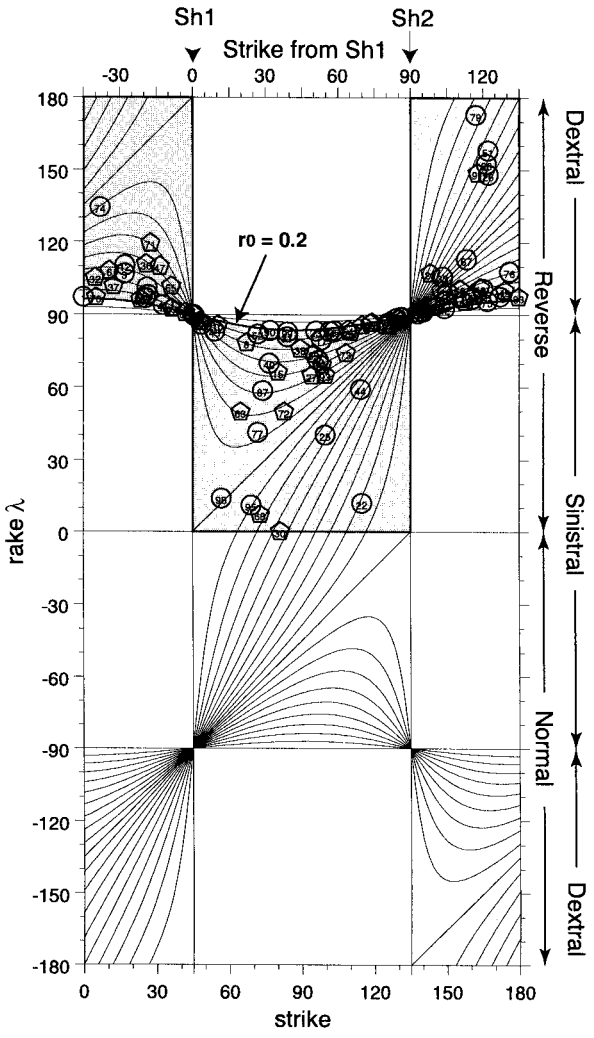

Fig. 14. Rake versus strike plot of data set C2 (Table 3) overlain by properly translated Breddin's graph of Fig. 9. Fault numbers shown within each symbol correspond to those of Fig. 11. Comparing same fault number with that of data set C8 (Fig. 13) show how much slip is getting closer to dip slip for the same fault plane orientation.

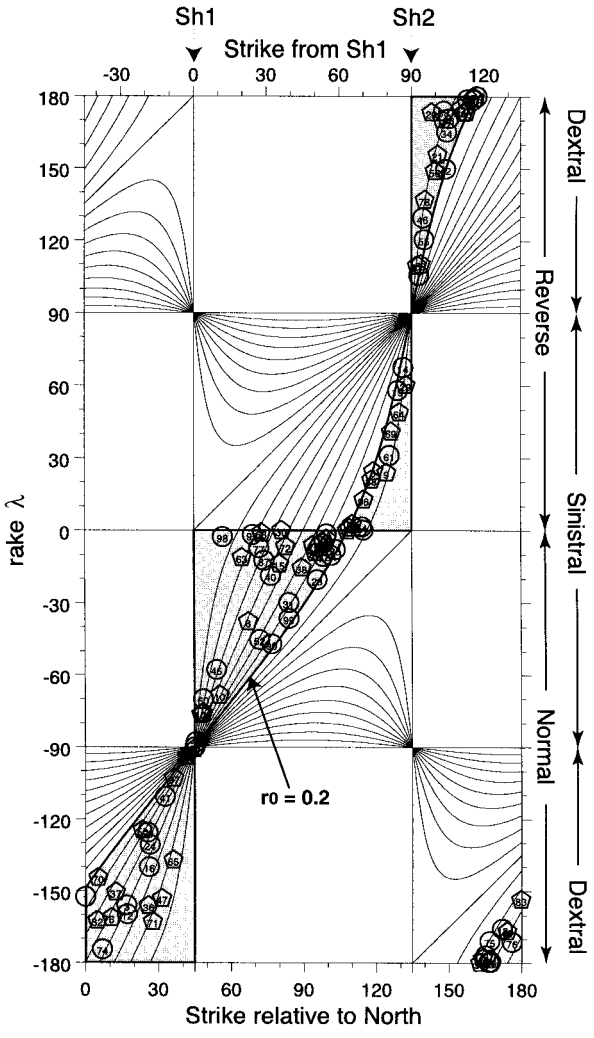

Fig. 15. Rake versus strike plot of data set W2 (Table 3) overlain by properly translated Breddin's graph of Fig. 9. Fault numbers shown within each symbol correspond to those of Fig. 11.

requires $r_0 \geq 0.2$ whereas the $NB_0(r_0, 2)$ fitting domain requires $r_0 \leq 0.2$. This tighter constraint is related to the fact that γ controls the transition from normal to reverse dip component of slip.

The above examples show that this graphical method requires a large strike dispersion of data in order to yield a usable constraint on the tectonic regime. In particular, a data set dominated by conjugate faults would not provide a good constraint on the stress tensor aspect ratio, r_0, because it does not provide fault planes striking away from the horizontal principal stress directions.

4. Application to natural data

4.1. Tectonic setting

A typical example of natural data with a large dispersion of strike is provided by the Vaulen outcrop of deformed Devonian conglomerate in the Solund basin of western Norway (Fig. 16). The conglomerate is made of coarse clasts (5 cm to 2 m) derived from the Precambrian–Early Palaeozoic basement and a sandy matrix that has been partially removed by weathering on a cliff. As a result protruding clasts display a large amount of their surface, which bear slickensides observed on planes of highly variable orientations (Fig. 17). A former analysis of these structures by the inversion technique of Etchecopar et al. (1981) revealed a well defined extensional phase that explains 80% of the data (Séranne, 1988, p.156) and that is nearly identical to that obtained from the analysis of micro faults from an outcrop a few hundred meters away (Fig. 16).

Regionally, a variety of meso-scale structural features within the Solund basin indicate strikingly consistent principal stress directions: a vertical compression and horizontal extension and intermediate axes oriented N120° and N030°

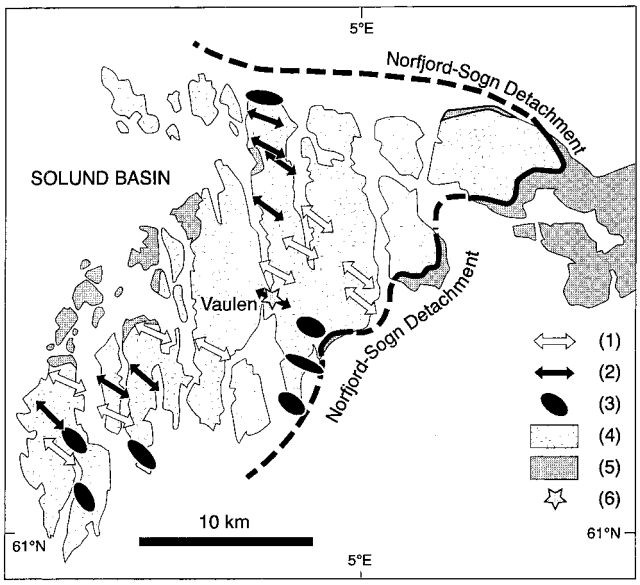

Fig. 16. Structural map of Solund Basin (modified after Séranne, 1988; Chauvet and Séranne, 1989). 1, minimum principal stress direction deduced from tension gashes; 2, minimum principal stress directions computed from striated microfaults; 3, strain ellipsoids from the ductile deformation of clasts close to the basal detachment; 4, Devonian conglomerate; 5, Early Palaeozoic basement; 6, Vaulen outcrop location.

respectively, that are interpreted to be associated with the basin formation (Séranne and Séguret, 1987; Séranne, 1988; Chauvet and Séranne, 1989). Deformation of the conglomerate of the Solund basin increases and becomes more ductile downwards and south-eastwards, toward the Norfjord–Sogn low-angle basal extensional detachment (Fig. 16). In the ductile and more deformed zone close to the detachment, clast axes ratio (long axes/short axes) increases, suggesting penetrative deformation. The Vaulen outcrop is located in the brittle, less deformed zone.

The assumption that the conglomerate slickensides can be explained by an homogeneous state of stress is limited, among other things, by the degree of rotation undergone by the pebbles. A preferred NW–SE orientation of clast long axes has indeed been observed and interpreted to be due in part to interclast rotation (Séranne and Séguret, 1987; Séranne, 1988; Chauvet and Séranne, 1989). However these rotations appear related to an early deformation that predates that associated with the slickensides. Later rotations remain possible but are expected to be of small magnitude. Thus even if the state of stress that deformed the conglomerate is well defined, a few incompatible slips are expected and some sorting is necessary.

4.2. Application of Breddin's graph

The rake versus strike plot show that normal slips are dominant, suggesting a dominant extensional regime (Fig. 18). The mixture of sinistral and dextral movement for similar strikes within the reverse slip data (included in the upper

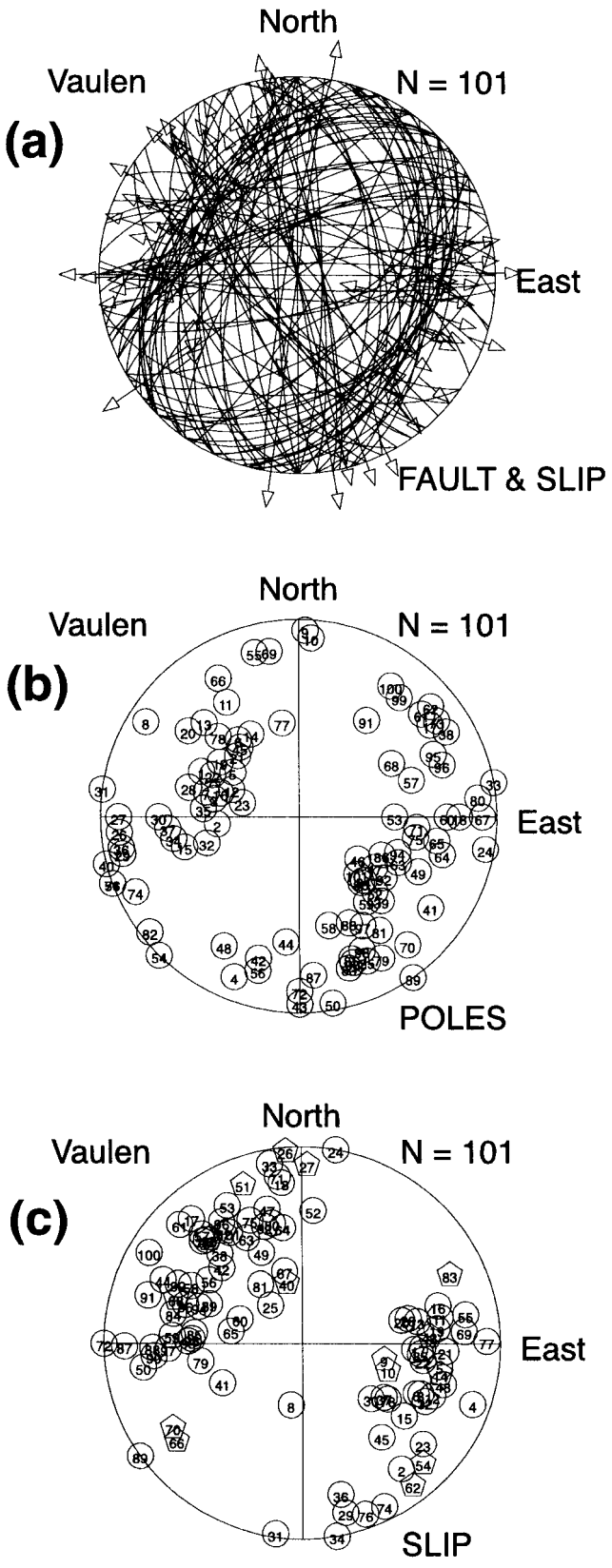

Fig. 17. Vaulen data stereographic projection (equal area projection, lower hemisphere). **(a)** Fault plane and slip. **(b)** Fault plane poles. **(c)** Slip vectors. Fault number is shown within each symbol. Location on Fig. 16.

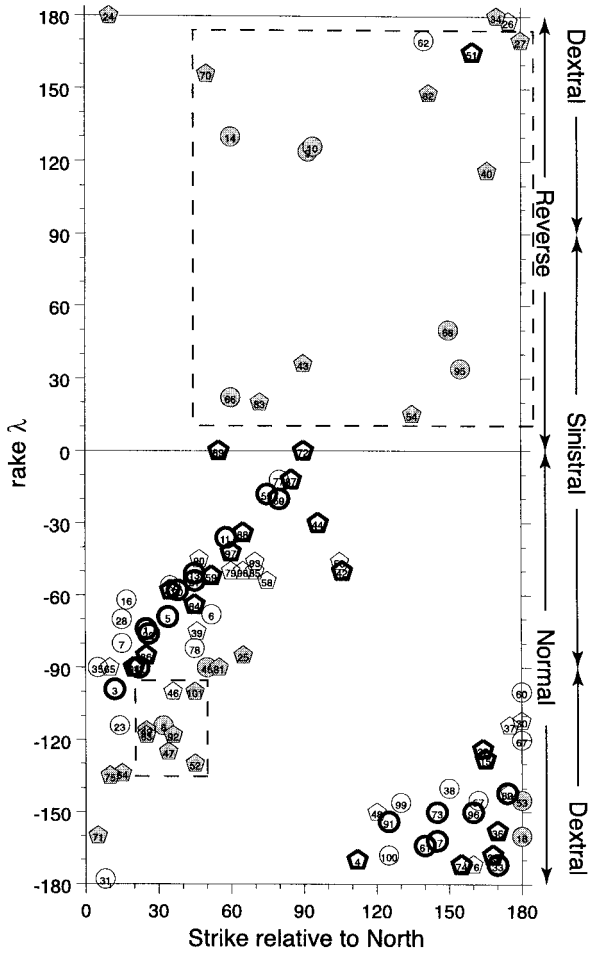

Fig. 18. Rake versus strike plot of the Vaulen data. Pentagons correspond to data with strike outside [0, 180°] that have been translated back into this interval by adding the correct multiple of 180°. Data with rake angular misfit higher than 30°, lower than 30° but higher than 10°, and lower than 10° with respect to stress tensor INV1 (Table 3) correspond to shaded symbols, open symbols and open symbols with thick contours, respectively. Dashed square: data excluded from the inversion yielding INV2 (Table 3). Fault numbers shown within each symbol correspond to those of Fig. 17.

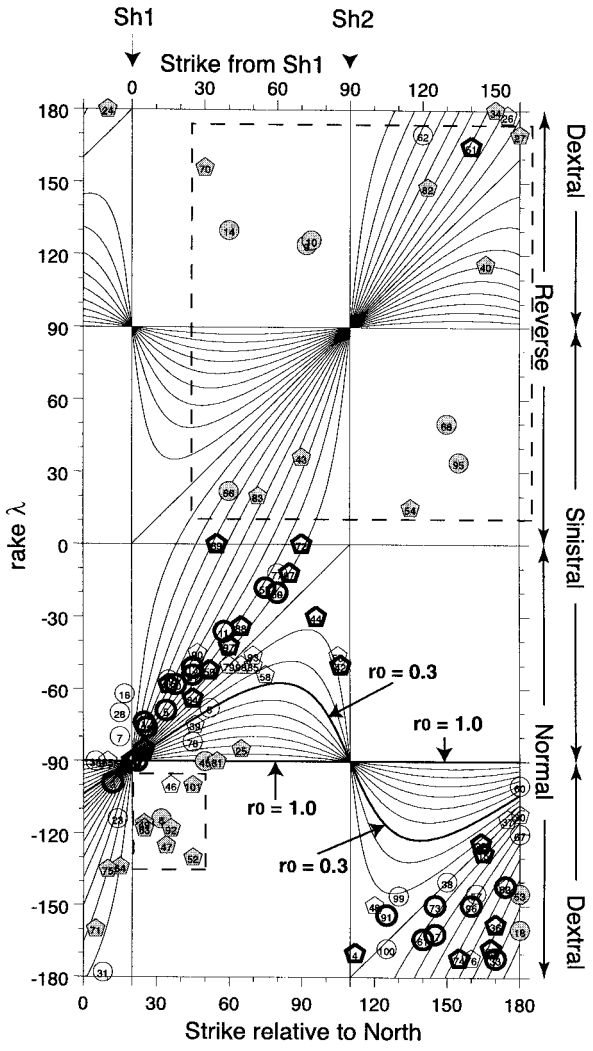

Fig. 19. Rake versus strike plot of the Vaulen data overlain by Breddin's graph. Same symbols as Fig. 18. The graphical interpretation yields the stress tensor BRED1 and BRED2 (Table 3).

dashed rectangle of Fig. 18) suggests that these data are not consistent with a single homogeneous stress system, which discounts searching for a secondary compressional phase to explain them.

The normal slip data show a clear separation between dextral and sinistral movements at strike of 110°. Overlaying the graph shows that most of these normal data are consistent with an extensional regime with a direction of horizontal extension at 110° (Fig. 19). The only clearly incompatible data are those with dextral movement striking between 20 and 50° (included in the lower dashed rectangle of Figs 18 and 19). Five steep normal sinistral slip data striking around 60° require radial extension with $r_0 = 1$ (Regime BRED1, Table 3). However if these five data are not considered, all the other data only require $r_0 = 0.3$ (Regime BRED2, Table 3).

4.3. Comparison with automatic stress inversion

A classical stress inversion was applied to the data set by using two computer programs: FAILLE (Etchecopar et al., 1981; Etchecopar, 1984) and FSA (Célérier, 1999), a program developed with similar inversion principles and with the addition of interactive graphics. A stress tensor that best explained 80% of the data was sought. The misfit criteria was chosen as the average of the absolute value of the angular difference between predicted and observed rakes. The resulting solution reduced stress tensor (Regime INV1, Table 3) is consistent with those inferred from Breddin's graph (Regime BRED1 and BRED2, Table 3), but for a lower r_0 value. To further analyse the INV1 solution, the angular misfit for each individual data are classified into three categories: misfit higher than 30°, lower than 30° but higher than 10°, lower than 10°, and marked accordingly on the rake versus strike plot (Figs 18, 19). There is a clear

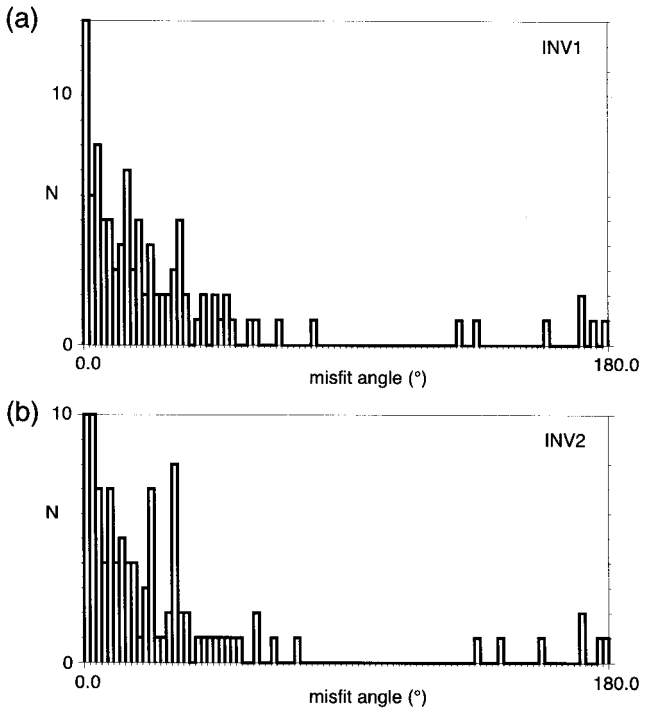

Fig. 20. Histogram of the rake angular misfit for the whole data set when (a) INV1 and (b) INV2 are applied. Histogram bin size is 2°.

tendency for the low misfits to cluster in the acceptable domains of Breddin's graph and for the high misfits to be out of them. This demonstrates that the automatic inversion technique has indeed focused its search on the same data as those selected by the graphic method. The inversion shows that the normal slip movements that dominate the data set are mechanically compatible with the INV1 solution tensor, which is then a natural solution, as inferred from Breddin's graph. However the inversion also demonstrates that grouping the data otherwise does not yield a better solution. Breddin's graph analysis suggested that much for a tensor with a near vertical principal stress but did not preclude alternate solutions with non vertical principal stress axes. The Breddin graph thus provides a representation of the compatibility of the data that helps understand the selection operated by the automatic inversion.

Part of the diverging results can be attributed to the fact that the inverse method search is not restricted to stress tensors with a vertical principal axis, as will be discussed further on. The lower r_0 ratio of INV1 is also related to high misfit of the five steep normal sinistral slip data striking around 60° mentioned above.

4.4. Selecting data before inverting

Another use of the graphic method is to help the selection of consistent subsets so as to apply the inversion in conditions closer to monophase data. The graph suggest that when looking for an extensional regime in the Vaulen data the data located within the dashed rectangles of Fig. 19 should not be considered, because they are not compatible with the dominant pattern. A data set was thus constructed by subtracting these data. An automatic stress inversion that required a best fit for 98% of this reduced data set yields the stress tensor INV2 (Table 3). The higher proportion of data, 98%, was required in the inversion because the data were already selected. The tensor INV2 is very similar to INV1 (Table 3) and when applied to the whole data set yields similar misfit angles as INV1 (Fig. 20). This shows that the selection done with the Breddin graph can to some extent replace that done internally by the automatic inversion procedure with the advantage of gaining some understanding on the compatible fault slip subsets.

5. Discussion

All that has been derived above does not really require one the principal stress axis to be vertical. The requirement is rather that the strike and rake be defined with respect to a reference frame that uses a principal stress axis. This means that one of the principal stress axes orientations must be known beforehand, and that this method only determines (1) which of the principal stress is along the known axis, (2) the rotation of the two other axes around the known axis, and (3) the stress tensor aspect ratio. This is the second underlying simplification that allows treatment of this three-dimensional problem in a manner almost as simple as the two-dimensional strain problem.

In practice, this implies that strike and rake data measured with respect to the geographical frame can be directly compared to the abacus only when one of the principal stress axes is close to the vertical.

If this is not the case, to apply this method would require recomputation of strike and rake with respect to a frame built around the principal stress axis with the steepest plunge. Using strike and rake data measured with respect to the geographical frame instead introduces an error which is exactly the difference between strike and rake between the two reference frames. These angular errors remain of the order of the angular deviation from the vertical of the principal stress axis with the steepest plunge for steeply dipping planes but can be much larger for planes with shallow dips. As a consequence, if the principal stress axis with the steepest plunge is not too deviated from the vertical, the method is expected to yield reasonable horizontal principal stress directions, because they are constrained by planes with steep dips, but poor estimate of the stress tensor aspect ratio, which is constrained by planes with shallow dips. The results obtained with the Vaulen data are consistent with this inference. In cases where the principal stress axis with the steepest plunge is strongly deviated from the vertical, applying inverse methods is clearly more appropriate.

6. Conclusion

Despite its limitations, the simplicity of this method make it attractive to assess the complexity of a data set, to infer the possible stress regimes in multi-phased data, and to help in the separation of the data in consistent subsets before applying the inversion procedure.

Acknowledgements

J. Angelier, L. Arlegui, and T Blenkinsop review comments helped improve the paper. We gratefully acknowledge the use of a modified version of P. Wessel's cal2ps PostScript Fortran library. This work was entirely supported by CNRS. Fsa and faille programs are available at http://www.isteem.univ-montp2.fr/PERSO/celerier/software/software.html

References

Aki, K., Richards, P.G., 1980. Quantitative seismology theory and methods. W.H. Freeman and Company, San Francisco.

Anderson, E.M., 1905. The dynamics of faulting. Transactions of the Edinburgh Geological Society 8, 387–402.

Angelier, J., 1984. Tectonic analysis of fault slip data sets. Journal of Geophysical Research 89, 5835–5848.

Armijo, R., Carey, E., Cisternas, A., 1982. The inverse problem in microtectonics and the separation of tectonic phases. Tectonophysics 82, 145–160.

Bott, M.H.P., 1959. The mechanics of oblique slip faulting. Geological Magazine 96, 109–117.

Breddin, H., 1956. Die tektnonische Deformation der Fossilien im Rheinischen Schiefergebirge. Zeitschrift der Deutschen Geologischen Gesellschaft 106, 227–305.

Bucher, W.H., 1920. The mechanical interpretation of joints: part I. Journal of Geology 28, 707–730.

Bucher, W.H., 1921. The mechanical interpretation of joints: part II. Journal of Geology 29, 1–28.

Carey, E., Brunier, B., 1974. Analyse théorique et numérique d'un modèle mécanique élémentaire appliqué à l'étude d'une population de failles. Comptes Rendus de l'Académie des Sciences, Série D 279, 891–894.

Célérier, B., 1988. How much does slip on a reactivated fault plane constrain the stress tensor? Tectonics 7, 1257–1278.

Célérier, B., 1995. Tectonic regime and slip orientation of reactivated faults. Geophysical Journal International 121, 143–191.

Célérier, B., 1999. FSA: Fault Slip Analysis software, http://www.isteem.univ-montp2.fr/PERSO/celerier/software/fsa.html.

Chauvet, A., Séranne, M., 1989. Microtectonic evidence of Devonian extensional westward shearing in southwest Norway. In: Gayer, R. (Ed.). The Caledonide Geology of Scandinavia. Graham & Trotman, London, pp. 245–254.

Etchecopar, A. 1984. Étude des états de contrainte en tectonique cassante et simulations de déformations plastiques (approche mathématique). Thèse d'État, Université des Sciences et Techniques du Languedoc.

Etchecopar, A., Vasseur, G., Daignieres, M., 1981. An inverse problem in microtectonics for the determination of stress tensors from fault striation analysis. Journal of Structural Geology 3, 51–65.

Fry, N., 1992. Stress ratio determination from striated faults: a spherical plot for cases of near vertical principal stress. Journal of Structural Geology 14, 1121–1131.

Fry, N., 1999. Striated faults: visual appreciation of their constraint on possible paleostress tensors. Journal of Structural Geology 21, 7–21.

Gephart, J.W., Forsyth, D.W., 1984. An improved method for determining the regional stress tensor using earthquake focal mechanism data: application to the San Fernando earthquake sequence. Journal of Geophysical Research 89, 9305–9320.

Guiraud, M., Laborde, O., Philip, H., 1989. Characterization of various types of deformation and their corresponding deviatoric stress tensors using microfault analysis. Tectonophysics 170, 289–316.

Harland, W.B., Bayly, M.B., 1958. Tectonic regimes. Geological Magazine 95, 89–104.

McKenzie, D.P., 1969. The relation between fault plane solutions for earthquakes and the directions of the principal stresses. Bulletin of the Seismological Society of America 59, 591–601.

Michael, A.J., 1984. Determination of stress from slip data: faults and folds. Journal of Geophysical Research 89, 11517–11526.

Philip, H., 1987. Plio-Quaternary evolution of the stress field in Mediterranean zones of subduction and collision. Annales Geophysicae 5B, 301–320.

Ramsay, J.G., Huber, M.I., 1985. The techniques of modern structural geology. Academic Press, London.

Reches, Z., 1987. Determination of the tectonic stress tensor from slip along faults that obey the Coulomb yield condition. Tectonics 6, 849–861.

Séranne, M. 1988. Tectonique des bassins dévoniens de Norvège: mise en évidence de bassins sédimentaires en extension formés par amincissement d'une croûte orogénique épaissie. Thèse Doctorat, Université des Sciences et Techniques du Languedoc.

Séranne, M. & Séguret, M. 1987. The Devonian Basins of western Norway: tectonics and kinematics of an extending crust. In: *Continental Extensional Tectonics* (edited by Coward, M. P., Dewey, J. F. & P.L., H.) Special Publication **28**. Geological Society of London, London, 37-48.

Simón Gómez, J.L., 1986. Analysis of a gradual change in stress regime (example from the Eastern Iberian chain, Spain). Tectonophysics 124, 37–53.

Vasseur, G., Etchecopar, A., Philip, H., 1983. Stress state inferred from multiple focal mechanisms. Annales Geophysicae 1, 291–298.

Wallace, R.E., 1951. Geometry of shearing stress and relation to faulting. Journal of Geology 59, 118–130.

Zoback, M.L., 1992. First- and second-order patterns of stress in the lithosphere: The world stress map project. Journal of Geophysical Research 97(B8), 11,703–11,728.